NANO · MICRO small
www.small-journal.com

Stress-Driven Grain Boundary Structural Transition in Diamond by Machine Learning Potential

*Chenchen Lu, Zhen Li, Xinxin Sang, Zheyong Fan, Xujun Xu, Yingyan Zhang, Ke Xu, Yanhua Cheng, Junhua Zhao, Jin-Cheng Zheng, and Ning Wei**

Understanding the structural dynamics of carbon grain boundaries, particularly in diamond, is essential for advancing next-generation device applications. Carbon's diverse allotropes, driven by its versatile chemical bonding, hold immense potential, yet analyzing these boundaries is challenging due to the limitations of experimental techniques and the computational demands of ab initio molecular dynamics simulations. In this study, a machine learning-based molecular dynamics potential, rigorously trained on ab initio data, that accurately predicts structural transitions in incoherent twin boundaries within diamond is introduced. This potential reveals the atomic-scale mechanisms driving these transitions and identifies an 80% reduction in interfacial thermal conductance during the grain boundary transition. These findings provide deep insights into the complex behavior of diamond grain boundaries, uncovering a novel mechanism that regulates thermal properties and paving the way for enhanced thermal management in diamond-based technologies.

1. Introduction

Grain boundaries (GBs), prevalent planar defects in polycrystalline materials, play a crucial role in determining the mechanical, thermal, and electrical properties of these materials.[1–4] Over the past few decades, GBs have emerged as a focus in the fields of solid-state physics and materials science due to their huge potential to manipulate material properties at the nanoscale.[5–7] For example, polycrystalline graphene has been shown to exhibit greater strength than pristine graphene sheets by alleviating the stress distribution around the GB structures.[8] This behavior can be well explained by continuum mechanics theory and molecular dynamics (MD) methods.[9,10] Furthermore, the Hall-Petch relationship illustrates how strengthening mechanisms (e.g. dislocation pile-ups at GBs) impede dislocation motion. This relationship suggests that plastic deformation is more difficult in materials with smaller grains and higher GB density.[11–13] In contrast, when the grain size is below 10 to 30 nm, the inverse Hall-Petch relationship occurs,[14] and the observed softening phenomena are attributed to GB migration, GB sliding, or grain rotation, as confirmed by experimental measurements and MD simulations.[15–18] Moreover, understanding GB-mediated processes such as migration, sliding, and transition is essential for achieving the properties of polycrystal through mechanical processing.[19–21]

C. Lu, Z. Li, X. Xu, J. Zhao, N. Wei
Jiangsu Key Laboratory of Advanced Food Manufacturing Equipment and Technology; Jiangsu Province Engineering Research Center of Micro-Nano Additive and Subtractive Manufacturing
Institute of Advanced Technology
Jiangnan University
Wuxi, Jiangsu 214122, P. R. China
E-mail: weining@jiangnan.edu.cn

X. Sang
Key Laboratory of Synthetic and Biological Colloids
Ministry of Education
School of Chemical and Material Engineering
Jiangnan University
Wuxi, Jiangsu 214122, P. R. China

X. Sang
International Research Center for Photoresponsive Molecules and Materials
Jiangnan University
Wuxi, Jiangsu 214122, P. R. China

The ORCID identification number(s) for the author(s) of this article can be found under https://doi.org/10.1002/smll.202409092

DOI: 10.1002/smll.202409092

Z. Fan
College of Physical Science and Technology
Bohai University
Jinzhou, Liaoning 121013, P. R. China

Y. Zhang
School of Engineering
RMIT University
PO Box 71, Bundoora, VIC 3083, Australia

K. Xu
Department of Electronic Engineering and Materials Science and Technology Research Center
The Chinese University of Hong Kong
Shatin, Hong Kong N.T. 999077, P. R. China

Y. Cheng
State Key Laboratory for Modification of Chemical Fibers and Polymer Materials
College of Materials Science and Engineering
Donghua University
Shanghai 201620, P. R. China

J.-C. Zheng
Department of Physics
Xiamen University
Xiamen, Fujian 361005, P. R. China

The structural transition and migration of GBs in metallic systems are crucial determinants of mechanical properties including strength, ductility, and resistance to various forms of degradation, such as creep and fatigue. These transitions can significantly hinder dislocation motion, thereby contributing substantially to the material's strengthening and hardening processes.[18,22–24] The introduction of coherent nanoscale internal boundaries has been shown to significantly increase material strength while maintaining or improving ductility.[25] In electroplated copper, the incorporation of a large amount of nanoscale twins drastically enhances strength without compromising the electrical conductivity.[24] This improvement is largely realized by engineering coherent nanoscale GBs. Clearly, detailed characterization of GB structures and transition mechanisms have been essential in refining GB engineering approaches for advanced materials development. Advanced imaging techniques have provided useful insights into GB structures, as seen in copper, where atomic-resolution imaging reveals the coexistence of two distinct structures and demonstrates the transformation from the metastable domino phase to the more stable pearl phase.[26] Observed in BCC-Fe metals, a transformation is facilitated by GB dislocation. A mechanism of plastic deformation associated with shear-coupled GB migration of {112} tilt GBs and vicinal GBs was proposed.[27] Furthermore, vacancies aid GB migration by reducing the line tension of the broken loops and serving as energetically favorable nucleation sites that facilitate GB disconnections.[28] In-situ observations have also recorded GB transformation induced by dislocation climb in nanostructured metals.[29] Those studies provide a novel approach to regulate the metal materials properties by exploring the metallic GB transformation, migration, and structural design.

Although there are numerous studies on the migration and structural transformations of metallic GB structures, studies on covalent materials remain rare.[30–32] This is attributed to the stability of covalent bonds, which are stronger than metallic and ionic bonds and require more stringent conditions for bond breaking and formation.[22] A recent groundbreaking study observed incoherent twin boundary configurations and structural transitions in diamonds.[33] Employing scanning transmission electron microscopy (STEM), researchers provided atomic-resolution insights into distinct {112} incoherent twin boundary configurations, as well as stress-driven transitions and configuration-dependent migrations in nanotwinned diamonds at room temperature. This pioneering research improves our understanding of incoherent twin boundaries in covalent materials. However, capturing the detailed structural properties during the GB transition remains a challenge due to limitations in experimental observations.

MD simulations are an effective tool for providing critical insights into the atomic-scale mechanisms, particularly overcoming the observational limitations of experiments. It provides a comprehensive view of material responses, captures intricate details of atomic motion, and unveiling complex deformation mechanisms beyond the reach of experimental methods. In the study of GBs, MD simulations have provided insights into the migration and transformation of GBs affected by transformation rates, temperature, and GB phase junction lengths. The coexistence and transformation dynamics of these GB phases were further elucidated through evolutionary GB structure search and clustering analysis.[26] In another MD study, the evolution of GBs revealed a metastable state in polycrystalline pure copper with grain sizes of a few nanometers.[34] An investigation into the mechanisms of GB migration in nanocrystalline copper highlighted the influence of temperature and grain size on migration rates and patterns.[35] MD simulations focusing on GB variations have revealed mechanisms that affect material properties, such as mechanical behaviors,[36,37] creep behaviors,[38] the impact of alloying elements,[39] and the type of GB structures.[40] All these MD simulation results complement experimental findings and offer insight into the GB behaviors at the atomic scale.

Recently, machine learning techniques have introduced a new paradigm for developing interatomic potentials.[41–46] In machine-learned potentials (MLPs), interatomic interactions are modeled using ML methods. This approach allows for a significantly larger number of fitting parameters, making MLPs more versatile than traditional many-body potentials. The basic theory behind MLPs is now well-established. MLPs consist of two main components: the regression model and the input descriptors. Input descriptors capture the atomic environment and serve as inputs to the regression model. Linearly complete basis functions have been proposed for constructing these descriptors.[47,48] For regression, various models have been successfully employed, including linear regression,[47,49] artificial neural networks (ANN),[50] and kernel-based regression.[51] Unlike traditional potentials, which rely on a limited set of analytical functions based on physical or chemical intuition, MLPs use highly flexible functional forms. These forms are not constrained to ground-state properties and enable MLPs to achieve accuracy levels far beyond those of traditional potentials.

Here, we focus on the microscopic processes and underlying physical mechanisms behind the GB structural transitions in diamond. We perform extensive MD simulations based on an accurate and highly efficient machine-learned interatomic potential[52] constructed within the neuroevolution potential framework.[53] GB transitions in diamonds are observed under shear loading consistent with those observed in the experiments.[33] This consistency provides a foundation for investigating the structural properties during the transition process. We detail the variations in atoms and bonds during the transition and measure key structural properties, including the number of bonds, atomic stress distribution, and the radial distribution function (RDF) at the GB interface which are beyond the reach of the experiment. Additionally, we identify significant changes in interfacial thermal conductance (ITC) during the GB transitions. In-depth analysis of the microscopic mechanisms and structural properties of covalent GB transitions in diamonds is provided to enable a new design platform for manipulating diamonds.

2. Results and Discussion

2.1. The Machine Learning Potential Training

Due to the complex nature of the diamond GBs which contain both sp^2 and sp^3 hybridization, an accurate force field is required in MD simulations to well describe the complex bonding and the bond-breaking and reforming. MLPs have emerged as a powerful tool in modeling the complex interactions in materials. The recently proposed neuroevolution potential (NEP) framework [54,55]

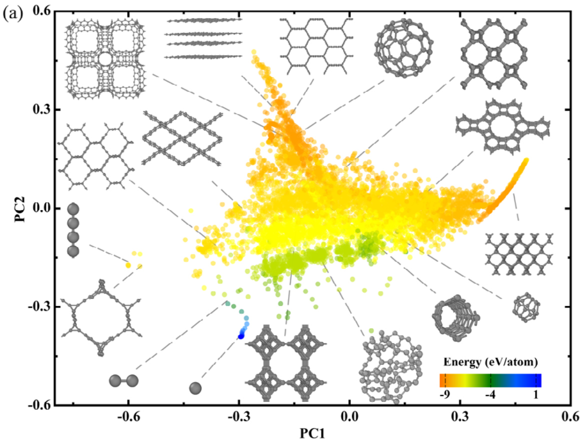

Figure 1. The MLPs training dataset. Overview of several the key structures from the training set, represented through a sketch map derived from principal component analysis of the learned descriptors. The color bar indicates the energy per atom in every structure.

is highly computationally efficient and has also been shown to achieve high accuracy for various forms of carbon.[56–58] The quality of any machine learning model depends on the quality of its input data. In this work, we adopt an NEP model trained using a very abundant set of structures as used to construct a Gaussian approximation potential model.[59] This dataset contains various carbon allotropes and defective configurations, totaling 6088 cells, each containing 1 to 240 atoms. MLPs constructed based on this dataset have been widely employed to investigate mechanical and thermal properties of various carbon systems.[52,60–62]

We provide an overview by visualizing its composition in **Figure 1a**. It allows us to identify several aspects of the constituent parts of the training database. By using the first and second main principal component analysis, the sketch map presents the data set virtually. The variance covered by these two components is 55.8% and 17.7%, respectively. It illustrates the instantaneous evolution of various parameters defined in the loss function during the training process (Figure S1a, Supporting Information). Notably, the root mean square errors (RMSEs) for energy, force, and virial stop declining at $\approx 5 \times 10^5$ steps, and completely converged after the training process. We have conducted a comparative analysis of the energy, force, and virial computed through the NEP approach and the corresponding results obtained from DFT calculations (Figure S1b–d, Supporting Information). From the distribution of the results in the diagonal graph, the results of NEP and DFT are very close, with RMSEs of 45 meV per atom, 599 meV Å^{-1}, and 105 meV per atom for energy, force, and virial, respectively. The errors from the Tersoff and adaptive intermolecular reactive bond order (AIREBO) potential are significantly larger than our NEP (shown in Figure S2, Supporting Information).

Accurately predicting the material properties of bulk crystalline phases is crucial for any potential model. We have compared the lattice parameters predicted by NEP with those obtained from the reference DFT method and several empirical models (Table S1, Supporting Information). Additionally, we evaluated the energies of various defects as calculated using DFT, NEP, and the other models considered (Table S2, Supporting Information). NEP demonstrates a high degree of accuracy, predicting defect formation energies within a 10% error margin in most cases. However, the errors for the formation energies of diamond defects are larger, ranging from 18% to 27%, while those for defective nanotubes range from 0% to 13%. Overall, NEP accurately models both the energetics and structural characteristics of a broad spectrum of carbon defects, highlighting its potential for diverse simulations involving defective structures, such as fracture, atom bombardment, and membrane characteristic simulations. We also use the training and test datasets for the carbon system to compare the NEP approach with other MLPs in terms of accuracy, speed, and memory usage. The MLPs to be compared include DP,[63] GAP,[51] MTP,[47] and REANN.[64] For all MLPs, we list the root mean square errors (RMSEs) for energies, forces, and virials (Table S3, Supporting Information). The NEP achieves a low force RMSE while maintaining the lowest computational cost. (Figure S3, Supporting Information). Furthermore, we compared the computational efficiency of NEP with traditional empirical potentials (Tersoff and AIREBO), as shown in Figure S4 (Supporting Information). While NEP improves computational efficiency by an order of magnitude compared to other machine-learning potentials, it is still an order of magnitude slower than Tersoff. As computational resources and algorithms continue to improve, we believe that MLPs will become powerful tools for the design, synthesis, and performance optimization of carbon-based nanomaterials. It shows that data-driven methods are indispensable for advancing cutting-edge research in materials science.

2.2. Transition of the GB Structure in Nanodiamond

In this work, MD methods and machine learning-based potential functions were employed to replicate the microscopic processes of the transition of covalent GB structures under shear stress as evidenced in a recent experimental work for the very first time.[33] In diamond nanocrystals, multiple twin boundaries formed by {111} and {112} planes are present, as shown in **Figure 2a**. The atomic structures at these interfaces were observed using STEM, particularly focusing on three typical covalent twin boundaries formed by the {112} planes in Figure 2b1–3, where the highlighted sections indicate the GB structures at the twin interfaces. Based on the microscopic atomic structures observed, corresponding atomic models of the covalent twin boundaries were established, with the GB structures highlighted by orange atoms in Figure 2c1–3.

During the experiments, the transition of the GB structure from Figure 2b1,2 was observed, with the specific dynamic transition process depicted in Figure 2d1–3. These images sequentially show the transition from the initial GB structure (Figure 2d1), through an intermediate state of partial structural transition (Figure 2d2), to the final complete transition (Figure 2d3). This experiment provides a valuable benchmark to validate the accuracy and generalizability of our machine-learned potential. It revealed the behavior of carbon materials under extreme conditions and offered critical experimental data for testing theoretical predictions. This has been essential for validating and advancing our new atomic interaction potential. The NEP was utilized in

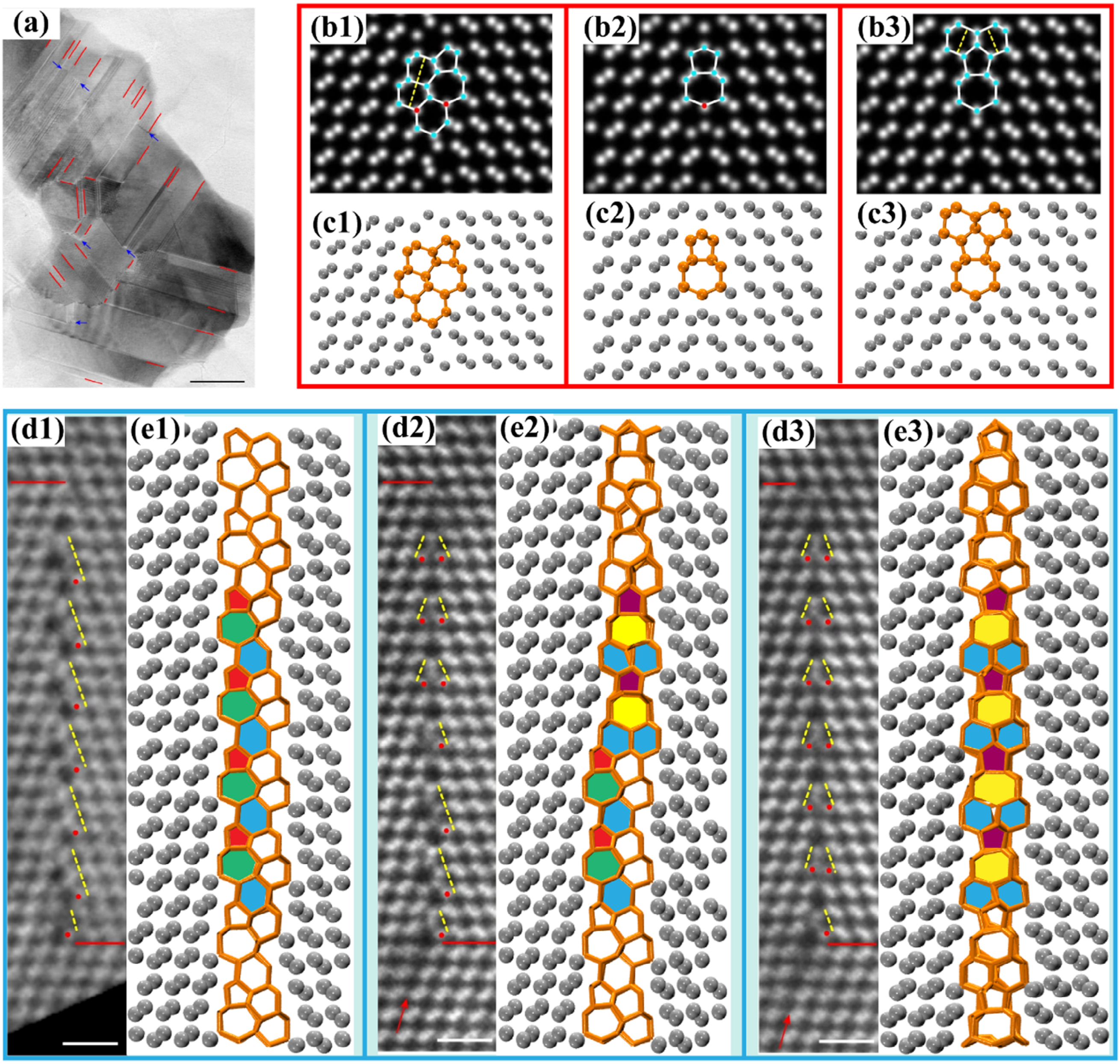

Figure 2. Twin boundary structures and transition in diamond. a) STEM image shows numerous {111} coherent twinning boundaries alongside {112} incoherent twin boundaries. b1–b3) HAADF-STEM images with corresponding structural models for three ITBs configurations. c1–c3) Atomic models are depicted. The structural units within the simulated images are highlighted by orange atoms. d1–d3) Sequence capturing the transition from configuration b1 to b2, illustrating the dynamic process from the initial state d1, through a partial transition state as an intermediate d2, to the final state d3. e1–e3) MD simulation of the dynamic process. The transition of GB structures is marked by different colors within carbon rings. a, b1–b3, and d1–d3 reprinted from Tong et al.,[33] copyright from 2024 Springer Nature.

MD simulations to replicate the transition of the GB structure, with snapshots of the dynamic process shown in Figure 2e1–3. In these images, grey atoms represent the diamond bulk structure, and orange covalent bonds indicate the GB structure. Carbon rings filled with different colors were used to highlight and distinguish the GB structures during the transition process.

In this study, different potential functions were employed to explore the transition process of GB structures under shear stress in diamond covalent twin boundaries. Three typical structural snapshots from the GB transition movies[33] are shown in **Figure 3**a1–a3. The dynamic process of GB transition under shear loading was simulated using three potentials: NEP (Figure 3b), Tersoff (Figure 3e), and AIREBO (Figure 3f). For all the shear simulations, Figure 3e,f displays the front and side views of the atomic model, respectively. One end of the model is fixed and the other end is subjected to shear strain at a constant velocity along the [−110] direction. In the images, the diamond and GB structures are represented by gray and orange atoms.

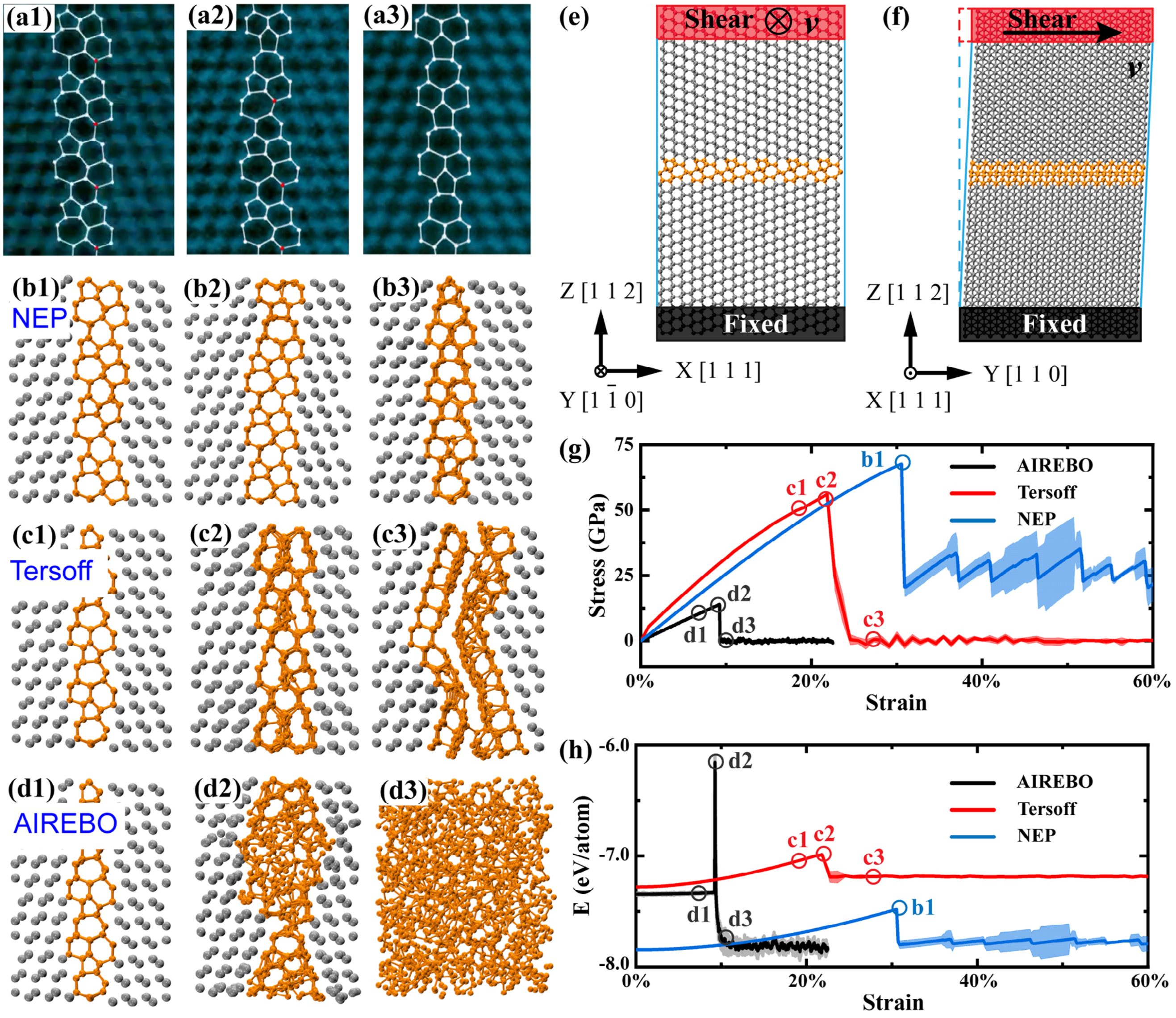

Figure 3. GB transition processes in diamond. a1–a3) STEM images capture the snapshots of the GB transition process a1–a3 reprinted from Tong et al.,[33] copyright from 2024 Springer Nature. b1,b2) Snapshots of three distinct states under shear loading, as conducted with the NEP potential. c1–c3) Representative snapshots under shearing, simulated using the Tersoff potential. d1–d3) The GB structure transitions to a disordered arrangement in simulations conducted with the AIREBO potential. e) Schematic representation of the diamond model with a GB setup for shear simulation. f) Side view of the shearing model. The atoms in the diamond bulk and diamond GB are colored gray and orange, respectively. g) Stress–strain curves for the diamond GB model under shear loading based on three different potentials. h) Variations in atomic energy within the GB structure under shear strain. Circles mark the corresponding snapshots in b–d, with the NEP potential indicated by blue circles, the Tersoff potential by red circles, and the AIREBO potential by black circles.

Using the same model subject to the simulation conditions, it is found that only the machine learning-based NEP[52] successfully replicates the structural transitions, while traditional interatomic potentials, including Tersoff[53] and AIREBO,[65] are unable to accurately capture the structural changes in the GB (Supporting Information Movies S1–S3, Supporting Information). Observations from experiments in Figure 3a1–3 indicate that the GB structure transition has undergone three stages: the initial state (Figure 3a1), the transitional state with partial structural transformation (Figure 3a2), and the final state of complete transition (Figure 3a3). In Figure 3b1–3, the snapshots from our MD simulations clearly display the same three stages of the transition process in the diamond covalent twin boundaries, consistent with the observed atomic structures shown in Figure 3a1–3 by experiments.[33]

However, MD simulations using the Tersoff potential function fail to capture the dynamic process of GB transition, as shown in Figure 3c1–3. Under shear loading, the initial GB interface began to distort due to the stress concentration. When the stress exceeds the strength threshold, the GB structure fails with bond breaking, and shear forces induce interlayer sliding. Likewise, MD simulations with AIREBO potential function[65] also fail to capture the GB structure transition. After reaching the stress peak, the atomic structure at the GB interface becomes disordered. The disordered structure propagates quickly from the interface and leads to the failure of the system.

The GB structural transition can be theoretically explained from the stress-strain and energy change curves (see Figure 3e,f). The stress values given by NEP exhibit a linear increase from 0 to 68 GPa with increasing strain. At the peak point, the atomic slippage induces the transition of the GB structure. The stress then drops suddenly to ≈25 GPa and fluctuates in a Zig-Zag format. This zigzag fluctuation indicates that the GB structure experiences reconstruction under shear strain rather than catastrophic failure. Furthermore, the Zig-Zag patterns observed in the atomic energy at the GB validate the process of transition. For the Tersoff and AIREBO potentials, as the shear strain increases, the stress gradually increases to the peak point, then drops dramatically to nearly zero, corresponding to a disordered atomic structure illustrated in Figure 3d3. While in the Tersoff potential simulations, the diamond structure remains almost unchanged but the GB structure fails. The shear loading causes sliding between twin diamond interfaces. Different colored circles in Figure 3g,h mark the atomic structures corresponding to the simulation results given by different potential functions used.

Our results show that training the potential on high-precision DFT data significantly improves its ability to describe complex physical phenomena. Unlike traditional empirical potentials, which rely on fixed functional forms, machine-learning-based potentials are more flexible and adaptable. They are particularly effective for nonequilibrium processes that traditional models cannot capture accurately.

2.3. Microstructural Properties of Nanodiamond GB Transition

Although experimental observations have successfully captured the process of GB transition, the microscopic mechanisms and structural properties of the atomic structure transition at the GBs remain unclear. However, MD simulations presented in the paper by Tong et al.[33] lack specific details, such as the atomic interaction potentials used in their simulations. Furthermore, the DFT calculations focus primarily on a quasi-static atomic migration process, which involves structural optimization rather than dynamic simulations. For this reason, the machine learning-based NEP was employed through MD simulations to systematically study the transition process of diamond GBs at the atomic scale by tracking the atomic trajectories during the shearing deformation process and analyzing the morphological change at the interface. **Figure 4**a1–7 displays the dynamic process of the GB atomic structure model (I–VII) under shear, while Figure 4b1–6 illustrates the micro-mechanisms of local atomic structure variations at the GB. In these snapshots, gray and yellow atoms represent the diamond and GB structures, respectively. The red and blue atoms highlight the broken and newly formed bonds, respectively.

The transition of the diamond GBs can be divided into two distinct stages. The first stage (I–IV) involves the breaking of covalent bonds at the GB due to shear stress, represented by red arrows and rectangular frames in the images. As shown in Figure 4b1–3, the concentrated stress at the GB leads to the breaking of covalent bonds. Initially, the covalent bonds break between the pentagon and heptagon carbon rings at the boundary, as shown in Figure 4b1. Subsequently, due to strain-induced atomic structural sliding, two sp^3 hybridized atoms transform into sp^2 hybridization, resulting in the breaking of two covalent bonds, as depicted in Figure 4b2. Finally, along the direction of the boundary transition, the diamond structure shifts to the GB structure, with two hexagonal carbon rings merging to form a single decagonal carbon ring, as illustrated in Figure 4b3. The second stage (IV–VII) is characterized by the formation of new covalent bonds with the slippage of atomic structure at the GB. In Figure 4b4–6, blue atoms represent the newly bonded atoms. The formation of a new bond at the GB turns a decagonal carbon ring into one pentagonal and one heptagonal carbon ring, as shown in Figure 4b4. The subsequent atomic structure slippage causes the two sp^2 hybridized atoms to transform into sp^3 hybridization, as shown in Figure 4b5. Eventually, Figure 4b6 illustrates that the original GB structure transforms into a diamond structure. At this point, the structural transition of the diamond covalent interface is completed. These detailed observations clearly elaborate the dynamic structural transition of diamond GBs under shear and reveal the underlying microscopic mechanisms. It provides important physical insights for better understanding of the GB structure transition process.

The variation in the proportion of carbon-carbon covalent bonds during the GB transition process corresponds to these two distinct stages of structural transition. As shown in Figure 4c, point I marks the peak stress in the GB structure, denoting the start of the transition. In the first stage, the covalent bonds are broken until the lowest point IV is reached. Subsequently, in the second stage, the shear loading induces atomic structural slippage, which in turn leads to the formation of new carbon-carbon covalent bonds. The proportion of covalent bonds keeps increasing until the transition of the GB structure stops at point VII. The noise in the curve is due to the asynchronous nature of the GB structural transitions. The local breaking and forming of bonds occur simultaneously, and the overall results of structural changes in GB are presented in Figure 4b1–6.

In addition, the atomic stress distribution and RDF of the GB structure are utilized to characterize the structural properties during the transition process. The distribution of atomic stress during the transition process is plotted in Figure 4d where the red arrow indicates changes in the position of peak stress. Figure 4e illustrates the variation of corresponding peak stress values with respect to strain. In the first stage, the peak stress values gradually increase with the increase of strain. This suggests that the increasing stress in the atomic structure drives the bond breaking at the GB interface. On one hand, the stress distribution curve becomes flatter because broken bonds release atomic stress. On the other hand, some atoms enhance the stress, as indicated by an increase in the peak stress value. Entering the second stage, due to atomic structure sliding and the formation of new covalent bonds, the peak shifts toward a lower stress direction. Similarly, the variations in the RDF of the GB structure also represent the dynamic process of structural transition. The changing trend of the RDF of the first nearest neighbor with respect to strain is shown in Figure 4f,g. During the bond-breaking stage of the GB structure, the RDF peak values of the first nearest neighbor gradually decrease. Due to the shear-induced breaking of

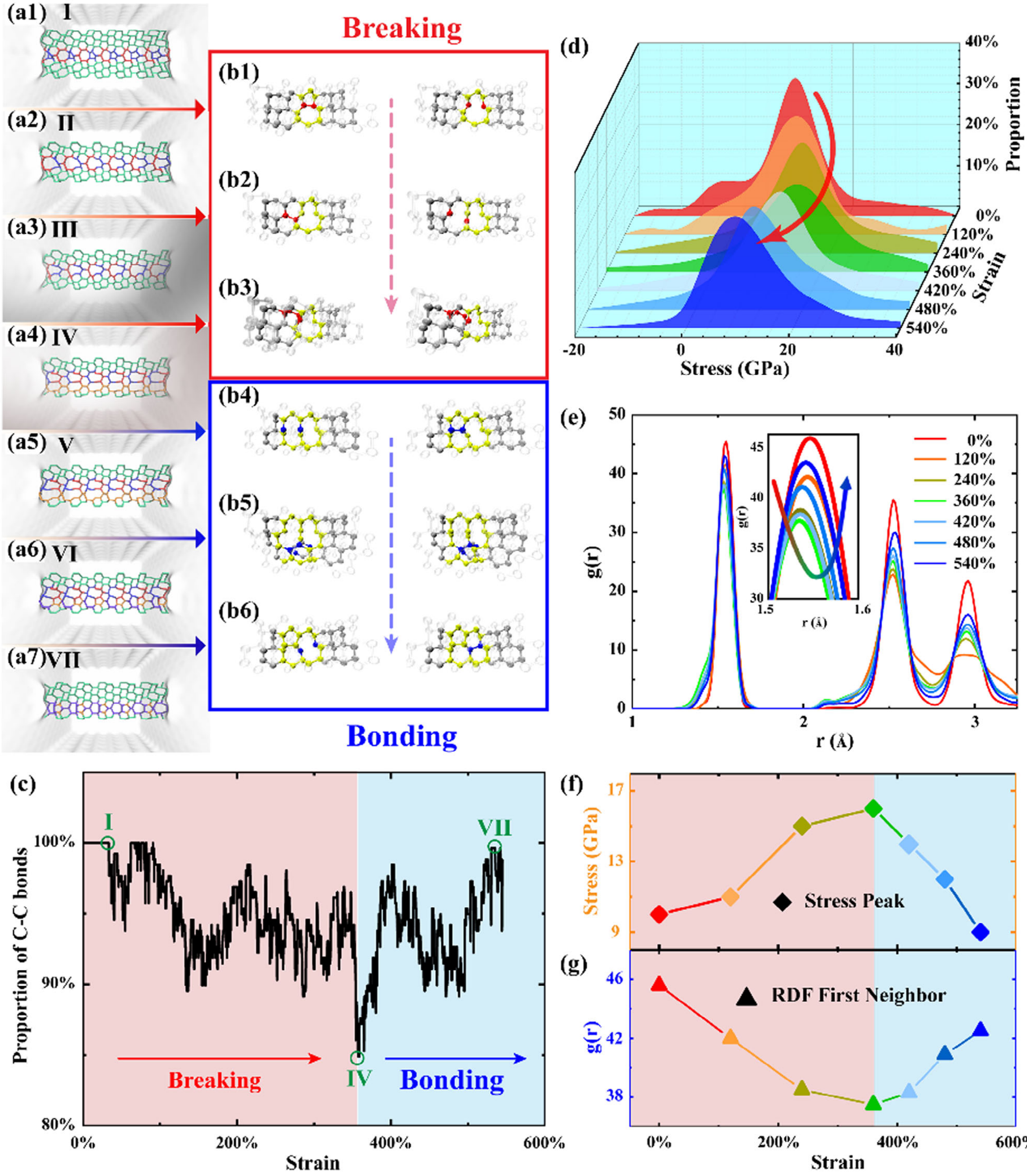

Figure 4. Atomic scale insights on structural properties. a1–a7) The ordering of these seven models of diamond GB structures (I–VII) illustrates the GB transition process. b1–b6) These panels reveal the local GB transitions within the atomic structures. Gray and yellow atoms denote the diamond and the GB structure, respectively. The red and blue atoms highlight the sites of bond breaking and bond formation, respectively. The transition states are divided into two stages: the bond-breaking phase is indicated by red squares, and the bond-forming phase is indicated by blue squares. c) The relative proportion of Carbon–Carbon bonds at the GB interface as a function of strain. Two transition states are characterized by bond breaking (red region) and bond forming (blue region). The initial state (I), the state with the lowest number of C—C bonds (IV), and the final state (VII) are indicated. d) Collection and analysis of atomic stress distribution in the GB structure under various strains, with the direction of the red arrow indicating the variation of stress peak. e) The RDF in the GB structure at different strains is depicted. An inset provides a detailed view of the first peak's shift. The arrow in the inset represents the change in peak value under different strain conditions. f) The values of the stress peak and g) the first neighbor in RDF are plotted. The same color coding in d–g) represents identical strain levels.

covalent bonds, the number of carbon-carbon covalent bonds is reduced. During the bond-forming stage of the GB structure, the atomic structure slides under shear stress, resulting in the formation of new covalent bonds. The first nearest neighbor peak values gradually increase until a new GB structure is formed.

The NEP-based MD simulations allow us to model the full dynamics of atomic motion and structural changes. This provides a clearer understanding of the atomic mechanisms behind grain boundary transitions. The method reveals subtle intermediate states that are difficult to observe experimentally. These findings overcome the limitations of traditional empirical potentials and enable researchers to study atomic-scale deformation mechanisms that experiments cannot capture. These results confirm the reliability of our potential and demonstrate its ability to explore complex dynamic behaviors in carbon crystals.

2.4. Thermal Property Monitoring of Nanodiamond GB Structural Transitions

Based on thermal property measurements, a detection scheme was proposed to elucidate the transition process of nanodiamond GB structures. Additionally, an in-depth analysis of the mechanisms affecting changes in thermal properties has been provided. A new mechanism for regulating the thermal properties of covalent interfaces has been proposed. Relying on STEM observations, experimental methods for identifying transitions in diamond GB structures are rather limited, particularly in capturing atomic dynamic processes. At the micro and nanoscale, detecting stress and strain also poses numerous challenges. The calculations of the ITC during the GB transition process revealed that the relative change in interface thermal conductivity can reach 80%. Thereby, it suggests that monitoring thermal properties offers a potentially feasible solution for observing variations in GB structures. Previous studies have categorized the regulation of interface thermal properties into two types: interaction strength in van der Waals interfaces and structural deformation in covalent interfaces. This study has proposed a new mechanism by which the thermal properties of interfaces can be regulated through transitions in the diamond GBs structure.

We construct a diamond model with twin boundaries as depicted in **Figure** 5a. The X and Y directions have periodic boundaries, and the Z direction has fixed boundaries. The model is fixed at both ends in the Z direction, with the left side serving as a heat source and the right side as a heat sink. A heat flow is shown along the Z direction. A steady heat flow is set along the Z direction. The orange rectangular box displays the diamond twin boundaries. Figure 5a also shows the temperature distribution along the direction of heat conduction in the model under non-equilibrium steady-state conditions. A typical temperature jump occurs at the GB interface. During the GBs transition process, we establish three corresponding atomic models, as shown in Figure 5b1–3. The initial structure (I) and final structure (VII) are observed in experiments, while the structure (IV) was obtained by simulation.

In the microscopic process of GB structure transition under shear, the ITC is measured under various strain conditions. The variations in ITC correspond to the two stages of GB transition, as shown in Figure 5d. In the first stage, due to the breaking of covalent bonds within the GB structure, the ITC shows a decreasing trend, dropping by ≈80% relative to the initial state. In the second stage, as new covalent bonds form, the ITC gradually increases. Compared to the initial state, the thermal properties exhibit only ≈a 10% decrease when the GB transforms into a new structure. The three red stars mark the initial state (I), the state with the lowest ITC (IV), and the final state (VII). The distribution of non-equilibrium steady-state atomic heat flow in these three states is depicted in insets. The vector arrows are added to each atom to visualize the spatial distribution of the microscopic heat flux. The color of the arrows indicates the magnitude of the heat flux.[66]

Compared to the state with the lowest ITC, the diamond structure in the initial and final states exhibits higher heat flux. The phonon scattering occurs on atoms in the GB structure. Particularly in the state with the lowest ITC, the most severe damage at the interface structure intensifies local phonon scattering, which hinders atomic vibrations and reduces the transfer of thermal energy. As a consequence, ITC is significantly reduced. Figure 5c shows the phonon density of states (PDOS) at the GB and diamond structures under different strains. It is evident that structural variations affect the vibrational modes of interface phonons. The ITC is mainly attributed to the coupling of high-frequency vibration modes. During the GB structure transition, the peak frequency of the GB structure is initially red-shifted and then blue-shifted. A red-shift in phonon vibrational frequency causes the phonon softening, reducing phonon group velocity, and decreasing ITC, while a blue-shift has the opposite effect. The overlap factor S of PDOS between the diamond and GB structures is also calculated and shown in Figure 5d. S decreases first and then increases with strain, which is consistent with the changes in ITC.

The ITC results reveal a new mechanism for regulating the thermal properties of interfaces through the transition of diamond GB structures. The significant changes in ITC provide a potentially feasible method for monitoring the transition of diamond GB structures. Moreover, by systematically studying interface phonon scattering, atomic heat flux, and PDOS, a deeper analysis of the micro-mechanisms behind the changes in ITC caused by GB transition has been conducted.

3. Conclusion

In this work, we developed a precise molecular dynamics potential using a machine learning approach based on ab initio results, achieving RMSEs significantly smaller than those of empirical potentials. We have constructed a {112} plane twin boundary diamond model to validate the GB transition observed experimentally under shear loading by using a machine learning-based NEP model combined with MD simulations. Our results indicate that compared to typical empirical many-body potentials, such as Tersoff and AIREBO, only the NEP predictions are consistent with experimental observations, thus providing a foundation for studying dynamic structural properties during the transition process. Unlike the limited availability of the dynamics of transition in experimental observations, the MD simulations based on NEP provide great details of transition at atomic scale, which facilitates better understanding of the underlying mechanisms of dynamic transition and the associated materials properties. Throughout the GB structure transition process, we quantified the proportion of bonds, the distribution of atomic stress, and the RDF, for a

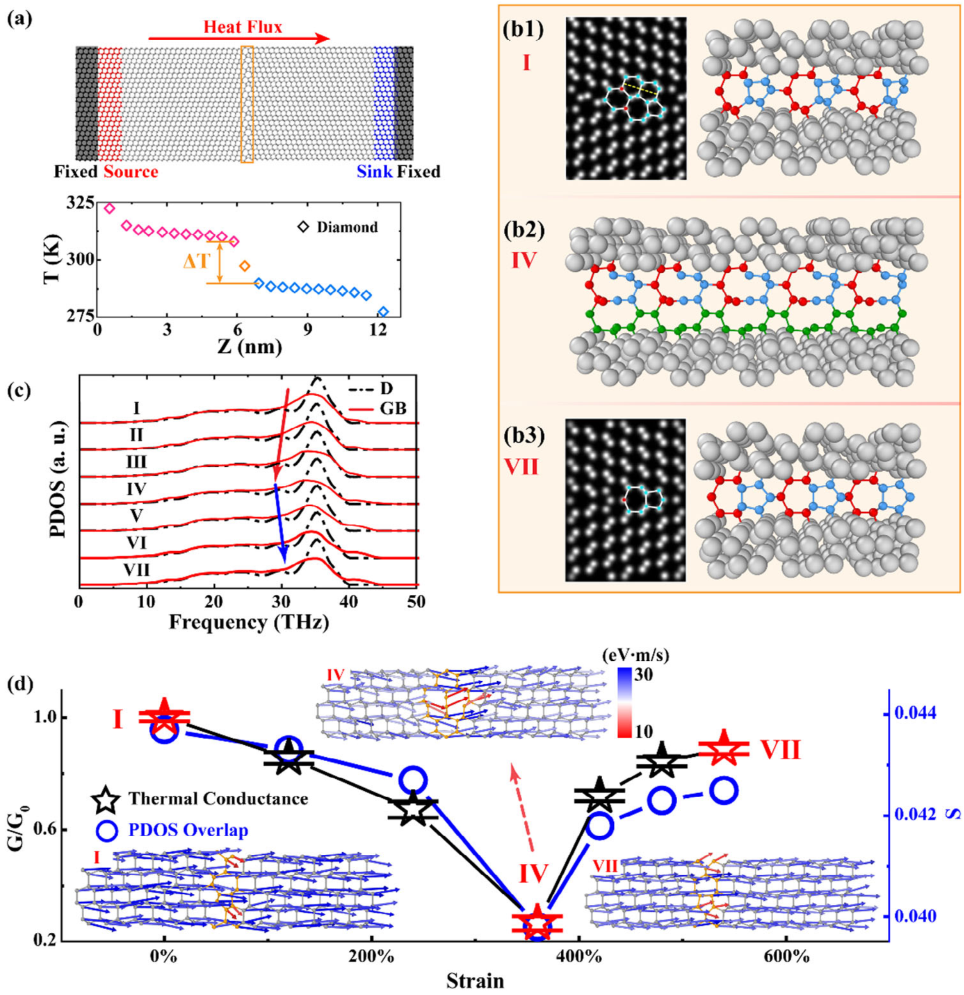

Figure 5. Thermal properties during GB transitions. a) Schematic representation of the setup for the NEMD simulation. Typical temperature profiles for the diamond GB system, highlighting a temperature discontinuity at the GB. A temperature jump occurs GB structure. b) Modeling of three ITB configurations (I, IV, and VII) during transition process. The inset reprinted from Tong et al.,[33] copyright from 2024 Springer Nature. c) DOS variations at the diamond and GB under shear loading, with arrows pointing to the red-shift and blue-shift in PDOS peaks at GB interfaces. d) ITC variations under different shear strains, alongside changes in the overlap factor S. Red stars indicate the initial state (I), the state with the lowest ITC (IV), and the final state (VII). Visualization of the spatial distribution of micro heat fluxes, represented by vector arrows on each atom across three states under a non-equilibrium steady state. The color bar indicates heat flux values.

clear view of two stages, i.e. bond breaking and formation. We have observed that the ITC values show a decrease-then-increase trend, with a maximum reduction of ≈80% at the bond-breaking stage of GB structures. This significant change in ITC can serve as a sensitive monitor for structural transitions. Our findings provide valuable insights into the microscopic mechanisms and structural properties of covalent GB transitions in diamond, offering strategic guidance for the regulation and application of polycrystalline materials.

4. Experimental Section

MD Simulations of GB Transition: During shear simulations, periodic boundary conditions were applied along both shear planar directions. The non-periodic boundary conditions were applied perpendicular to the shear plane. The system underwent an initial relaxation in the isothermal-isobaric (NPT) ensemble at a temperature of 300 K and zero external pressure, using a Berendsen thermostat and barostat[67] for 1.0 ns. Subsequently, the NPT ensemble was replaced by the canonical (NVT) ensemble realized by the Berendsen thermostat[67] to carry out shear simulation. In the shear deformation, a constant shear velocity parallel to the boundary plane was applied on the fixed area of the upper grain along the [1−9,10] direction at 300 K while fixing a few atom layers at the end of the bottom grain. All the MLP-based MD simulations were performed using the open-source graphics processing units molecular dynamics (GPUMD) package[68] with a time step of 0.5 fs. The MD simulations with the Tersoff[53] and AIREBO[65] potential were performed by using the open-source large-scale atomic/molecular massively parallel simulator (LAMMPS) package.[69]

MD simulations of ITC at GB Structures: The NEMD method is commonly employed to evaluate thermal properties. It follows Fourier's law by partitioning the system into three regions: a perpetual heat source providing energy, a heat sink continually dissipating energy, and a free sector for transporting thermal energy. As energy is transferred from the thermostat to the atoms within the heat source region, the thermostat's energy coupling to this region decreases. Conversely, in the heat sink region, the energy coupling of the thermostat increases as energy transfers from the atoms to the thermostat. The system, excluding the fixed regions, is initially equilibrated in an NVT ensemble at 300K for 1.0 ns. Then, the system is switched to a microcanonical (NVE) ensemble for heat transportation. Temperatures were controlled at 325 K in the heat source (Hot) region and 275 K in the heat sink (Cold) region using Langevin thermostats.[56] This setup causes a directional thermal energy transfer due to the temperature difference. A non-equilibrium steady state was reached when the temperature distribution was stabilized after 1.0 ns. Data collection starts after 5.0 ns. The energy transfer rate is calculated as:

$$J = \frac{dE(t)}{dt} \tag{1}$$

with E representing the energy of the hot and cold thermostats. ITC is determined by $G = J/A\Delta T$, where A is the heat transfer cross-sectional area and ΔT is the temperature difference between the heat source and sink. Five independent simulations are conducted for each model to ensure statistical accuracy, with the standard deviations represented by error bars. A detailed analysis of the sources of error and their impact on ITC is discussed (Appendix H, Supporting Information).

To further investigate the thermal transport mechanisms, a common method for calculating PDOS is to perform a Fourier transform on the velocity auto-correlation functions as follows:[70]

$$P(\omega) = \left(\int_0^{\infty} e^{i\omega t} \left\langle \sum_{j=1}^{N} v_j(t)\, v_j(0) \right\rangle d\omega \right) / \sqrt{2\pi} \tag{2}$$

where $P(\omega)$ is PDOS at frequency ω and $v_j(t)v_j(0)$ is the velocity auto-correlation function. Moreover, we quantify the overlap of the PDOS (represented by S) to indicate how well the phonon spectra match. S can be calculated as follows:[71]

$$S = \frac{\int_0^{\infty} P_{Diamond}(\omega)\, P_{GB}(\omega)\, d\omega}{\int_0^{\infty} P_{Diamond}(\omega)\, d\omega \int_0^{\infty} P_{GB}(\omega)\, d\omega} \tag{3}$$

where $P_{Diamond}(\omega)$ and $P_{GB}(\omega)$ denote the phonon spectra at frequency ω of diamond and GBs structure near the interface, respectively.

Supporting Information

Supporting Information is available from the Wiley Online Library or from the author.

Acknowledgements

This work was supported by the National Key R&D program of China (2023YFB4605101); National Natural Science Foundation of China (Grants Nos. 12372109, 12372327); State Key Laboratory for Modification of Chemical Fibers and Polymer Materials (Grant No. KF2211); Key Laboratory of Special Protective Textiles of Ministry of Education (Jiangnan University) No. TZFH-24-004; the 111 projects (Grant No. B18027). The authors would like to acknowledge Professor Zhi-Hui Li for reviewing the manuscript.

Conflict of Interest

The authors declare no conflict of interest.

Author Contributions

C.L. performed formal analysis, investigation, methodology, and visualization, wrote and reviewed the draft and edited the original manuscript, also performed data curation; Z.L. performed methodology, validation, and visualization, and wrote and reviewed the draft, and edited the original manuscript; X.S. performed conceptualization, acquired resources, and wrote the original draft and reviewed and edited the manuscript; Z.F. performed methodology, software, and wrote the original draft and reviewed, and edited the original manuscript; X.X. performed investigation and methodology; Y.Z. performed methodology wrote the original draft and reviewed also edited the manuscript; K.X. performed methodology, conceptualization, and wrote the draft and reviewed and edited the manuscript; Y.C. wrote the draft and reviewed and edited the manuscript; J.Z. performed conceptualization, acquired funding acquisition, resources, and supervised the work; J.-C.Z. wrote the draft and reviewed and edited the manuscript, and performed supervision; N.W. performed conceptualization, investigation, methodology, funding acquisition, and validation, wrote the draft and reviewed and edited the manuscript.

Data Availability Statement

The data that support the findings of this study are available from the corresponding author upon reasonable request.

Keywords

grain boundary transition, machine-learning potential, structural properties, thermal conductance

Received: October 4, 2024
Revised: February 19, 2025
Published online: March 7, 2025

[1] P. R. Cantwell, M. Tang, S. J. Dillon, J. Luo, G. S. Rohrer, M. P. Harmer, *Acta Mater.* **2014**, *62*, 1.
[2] S. J. Dillon, K. Tai, S. Chen, *Curr. Opin. Solid State Mater. Sci.* **2016**, *20*, 324.
[3] X.-W. Yi, Z. Zhang, Z.-W. Liao, X.-J. Dong, J.-Y. You, G. Su, *Nano Today* **2022**, *42*, 101346.
[4] H. Van Swygenhoven, J. R. Weertman, *Mater. Today* **2006**, *9*, 24.
[5] K. Lu, *Nat. Rev. Mater.* **2016**, *1*, 16019.
[6] C. Sealy, *Nano Today* **2023**, *52*, 101977.
[7] S. Chen, Z. H. Aitken, S. Pattamatta, Z. Wu, Z. G. Yu, D. J. Srolovitz, P. K. Liaw, Y.-W. Zhang, *Mater. Today* **2023**, *65*, 14.
[8] R. Grantab, V. B. Shenoy, R. S. Ruoff, *Science* **2010**, *330*, 946.
[9] Y. Wei, J. Wu, H. Yin, X. Shi, R. Yang, M. Dresselhaus, *Nat. Mater.* **2012**, *11*, 759.
[10] J. Wu, Y. Wei, *J. Mech. Phys. Solids* **2013**, *61*, 1421.
[11] C. Wang, K. Du, K. Song, X. Ye, L. Qi, S. He, D. Tang, N. Lu, H. Jin, F. Li, H. Ye, *Phys. Rev. Lett.* **2018**, *120*, 186102.
[12] E. O. Hall, *Proc. Phys. Soc. B* **1951**, *64*, 747.
[13] J. Chen, L. Lu, K. Lu, *Scr. Mater.* **2006**, *54*, 1913.
[14] M. A. Meyers, A. Mishra, D. J. Benson, *Prog. Mater. Sci.* **2006**, *51*, 427.
[15] Z. Shan, E. A. Stach, J. M. K. Wiezorek, J. A. Knapp, D. M. Follstaedt, S. X. Mao, *Science* **2004**, *305*, 654.
[16] T. J. Rupert, D. S. Gianola, Y. Gan, K. J. Hemker, *Science* **2009**, *326*, 1686.
[17] J. Schiøtz, K. W. Jacobsen, *Science* **2003**, *301*, 1357.
[18] J. Hu, Y. N. Shi, X. Sauvage, G. Sha, K. Lu, *Science* **2007**, *355*, 1292.
[19] J. Han, S. L. Thomas, D. J. Srolovitz, *Prog. Mater. Sci.* **2018**, *98*, 386.
[20] Z.-J. Wang, Q.-J. Li, Y. Li, L.-C. Huang, L. Lu, M. Dao, J. Li, E. Ma, S. Suresh, Z.-W. Shan, *Nat. Commun.* **2017**, *8*, 1108.
[21] N. C. Admal, G. Po, J. Marian, *Int. J. Plast.* **2018**, *106*, 1.
[22] Q. Huang, D. Yu, B. Xu, W. Hu, Y. Ma, Y. Wang, Z. Zhao, B. Wen, J. He, Z. Liu, Y. Tian, *Nature* **2014**, *510*, 250.

[23] T. Irifune, A. Kurio, S. Sakamoto, T. Inoue, H. Sumiya, *Nature* **2003**, *421*, 599.
[24] K. Lu, L. Lu, S. Suresh, *Science* **2009**, *324*, 349.
[25] L. Lu, Y. Shen, X. Chen, L. Qian, K. Lu, *Science* **2004**, *304*, 422.
[26] T. Meiners, T. Frolov, R. E. Rudd, G. Dehm, C. H. Liebscher, *Nature* **2020**, *579*, 375.
[27] N. Kvashin, P. L. García-Müller, N. Anento, A. Serra, *Phys. Rev. Mater.* **2020**, *4*, 073604.
[28] D. Chen, S. Xu, Y. Kulkarni, *Phys. Rev. Mater.* **2020**, *4*, 033602.
[29] S. Chu, P. Liu, Y. Zhang, X. Wang, S. Song, T. Zhu, Z. Zhang, X. Han, B. Sun, M. Chen, *Nat. Commun.* **2022**, *13*, 4151.
[30] A. T. Paxton, A. P. Sutton, *Acta Metall.* **1989**, *37*, 1693.
[31] H. Sawada, H. Ichinose, *Scr. Mater.* **2001**, *44*, 2327.
[32] H. Sawada, H. Ichinose, M. Kohyama, *J. Phys.: Condens. Matter* **2007**, *19*, 026223.
[33] K. Tong, X. Zhang, Z. Li, Y. Wang, K. Luo, C. Li, T. Jin, Y. Chang, S. Zhao, Y. Wu, Y. Gao, B. Li, G. Gao, Z. Zhao, L. Wang, A. Nie, D. Yu, Z. Liu, A. V. Soldatov, W. Hu, B. Xu, Y. Tian, *Nature* **2024**, *626*, 79.
[34] X. Y. Li, Z. H. Jin, X. Zhou, K. Lu, *Science* **2020**, *370*, 831.
[35] V. Yamakov, D. Wolf, S. R. Phillpot, A. K. Mukherjee, H. Gleiter, *Nat. Mater.* **2004**, *3*, 43.
[36] X. Li, Y. Wei, L. Lu, K. Lu, H. Gao, *Nature* **2010**, *464*, 877.
[37] Y. Mishin, M. Asta, J. Li, *Acta Mater.* **2010**, *58*, 1117.
[38] V. Yamakov, D. Wolf, S. R. Phillpot, H. Gleiter, *Acta Mater.* **2002**, *50*, 61.
[39] T. Frolov, S. V. Divinski, M. Asta, Y. Mishin, *Phys. Rev. Lett.* **2013**, *110*, 255502.
[40] F. Sansoz, J. F. Molinari, *Acta Mater.* **2005**, *53*, 1931.
[41] J. Behler, *J. Chem. Phys.* **2016**, *145*, 170901.
[42] V. L. Deringer, M. A. Caro, G. Csányi, *Adv. Mater.* **2019**, *31*, 1902765.
[43] T. Mueller, A. Hernandez, C. Wang, *J. Chem. Phys.* **2020**, *152*, 050902.
[44] Y. Mishin, *Acta Mater.* **2021**, *214*, 116980.
[45] O. T. Unke, S. Chmiela, H. E. Sauceda, M. Gastegger, I. Poltavsky, K. T. Schütt, A. Tkatchenko, K.-R. Müller, *Chem. Rev.* **2021**, *121*, 10142.
[46] F. Noé, A. Tkatchenko, K.-R. Müller, C. Clementi, *Annu. Rev. Phys. Chem.* **2020**, *71*, 361.
[47] A. V. Shapeev, *Multiscale Model. Simul.* **2016**, *14*, 1153.
[48] R. Drautz, *Phys. Rev. B* **2019**, *99*, 014104.
[49] A. P. Thompson, L. P. Swiler, C. R. Trott, S. M. Foiles, G. J. Tucker, *J. Comput. Phys.* **2015**, *285*, 316.
[50] J. Behler, M. Parrinello, *Phys. Rev. Lett.* **2007**, *98*, 146401.
[51] A. P. Bartók, M. C. Payne, R. Kondor, G. Csányi, *Phys. Rev. Lett.* **2010**, *104*, 136403.
[52] Z. Fan, Y. Xiao, Y. Wang, P. Ying, S. Chen, H. Dong, *J. Phys.: Condens. Matter* **2024**, *36*, 245901.
[53] J. Tersoff, *Phys. Rev. B* **1989**, *39*, 5566.
[54] Z. Fan, Z. Zeng, C. Zhang, Y. Wang, K. Song, H. Dong, Y. Chen, T. Ala-Nissila, *Phys. Rev. B* **2021**, *104*, 104309.
[55] Z. Fan, Y. Wang, P. Ying, K. Song, J. Wang, Y. Wang, Z. Zeng, K. Xu, E. Lindgren, J. M. Rahm, A. J. Gabourie, J. Liu, H. Dong, J. Wu, Y. Chen, Z. Zhong, J. Sun, P. Erhart, Y. Su, T. Ala-Nissila, *J. Chem. Phys.* **2022**, *157*, 114801.
[56] Z. Li, S. Xiong, C. Sievers, Y. Hu, Z. Fan, N. Wei, H. Bao, S. Chen, D. Donadio, T. Ala-Nissila, *J. Chem. Phys.* **2019**, *151*, 234105.
[57] P. Ying, H. Dong, T. Liang, Z. Fan, Z. Zhong, J. Zhang, *Extreme Mech. Lett.* **2023**, *58*, 101929.
[58] H. Dong, C. Cao, P. Ying, Z. Fan, P. Qian, Y. Su, *Int. J. Heat Mass Transfer* **2023**, *206*, 123943.
[59] P. Rowe, V. L. Deringer, P. Gasparotto, G. Csányi, A. Michaelides, *J. Chem. Phys.* **2020**, *153*, 034702.
[60] Y. Li, J.-W. Jiang, *Phys. Chem. Chem. Phys.* **2023**, *25*, 25629.
[61] G. A. Marchant, M. A. Caro, B. Karasulu, L. B. Pártay, *npj Comput. Mater.* **2023**, *9*, 131.
[62] B. Cheng, S. Hamel, M. Bethkenhagen, *Nat. Commun.* **2023**, *14*, 1104.
[63] H. Wang, L. Zhang, J. Han, W. E., *Comput. Phys. Commun.* **2018**, *228*, 178.
[64] Y. Zhang, J. Xia, B. Jiang, *Phys. Rev. Lett.* **2021**, *127*, 156002.
[65] S. J. Stuart, A. B. Tutein, J. A. Harrison, *J. Chem. Phys.* **2000**, *112*, 6472.
[66] Z. Fan, L. F. C. Pereira, H.-Q. Wang, J.-C. Zheng, D. Donadio, A. Harju, *Phys. Rev. B* **2015**, *92*, 094301.
[67] H. J. C. Berendsen, J. P. M. Postma, W. F. van Gunsteren, A. DiNola, J. R. Haak, *J. Chem. Phys.* **1984**, *81*, 3684.
[68] Z. Fan, C. Wei, V. Ville, H. Ari, *Comput. Phys. Commun.* **2017**, *218*, 10.
[69] S. Plimpton, *J. Comput. Phys.* **1995**, *117*, 1.
[70] J. M. Dickey, A. Paskin, *Phys. Rev.* **1969**, *188*, 1407.
[71] B. Li, J. Lan, L. Wang, *Phys. Rev. Lett.* **2005**, *95*, 104302.